PNAS RESEARCH ARTICLE | CELL BIOLOGY OPEN ACCESS

Spindle reorientation in response to mechanical stress is an emergent property of the spindle positioning mechanisms

Manasi Kelkar[a,1], Pierre Bohec[a], Matthew B. Smith[b], Varun Sreenivasan[c,d], Ana Lisica[a], Léo Valon[e], Emma Ferber[a], Buzz Baum[f,g,h], Guillaume Salbreux[b,i,1], and Guillaume Charras[a,h,j,1]

Edited by Rebecca Heald, University of California, Berkeley, CA; received December 3, 2021; accepted April 28, 2022

Proper orientation of the mitotic spindle plays a crucial role in embryos, during tissue development, and in adults, where it functions to dissipate mechanical stress to maintain tissue integrity and homeostasis. While mitotic spindles have been shown to reorient in response to external mechanical stresses, the subcellular cues that mediate spindle reorientation remain unclear. Here, we used a combination of optogenetics and computational modeling to investigate how mitotic spindles respond to inhomogeneous tension within the actomyosin cortex. Strikingly, we found that the optogenetic activation of RhoA only influences spindle orientation when it is induced at both poles of the cell. Under these conditions, the sudden local increase in cortical tension induced by RhoA activation reduces pulling forces exerted by cortical regulators on astral microtubules. This leads to a perturbation of the balance of torques exerted on the spindle, which causes it to rotate. Thus, spindle rotation in response to mechanical stress is an emergent phenomenon arising from the interaction between the spindle positioning machinery and the cell cortex.

cell cortex | optogenetics | RhoA | mechanics | spindle orientation

Significance

Precise control of spindle positioning is critical during developmental morphogenesis and homeostasis in epithelia. While mitotic spindles have been shown to reorient in response to external stresses, the subcellular cues that induce reorientation remain unclear. Here, by using a combination of optogenetics, molecular perturbations, and computational modeling, we investigate the spindle response to inhomogeneous tension in the actomyosin cortex. We show that a sudden local increase in RhoA activity and tension at cell poles leads to a perturbation of the torque balance acting on the spindle, causing it to rotate, subsequently affecting division orientation. Spindle reorientation may help optimize cell packing in tissues subjected to transient or cyclical deformations.

The orientation of the mitotic spindle determines the axis of cell division (1, 2). Cell division orientation must be carefully regulated during embryonic development to dictate proper cell fate as well as in adult organisms to maintain tissue homeostasis or enable adaptation to environmental changes (3–6). In tissues, division orientation has been shown to homogenize cell packing (7) and to prevent the buildup of excessive mechanical stress, which may endanger tissue integrity. In monolayered epithelia, cell divisions parallel to the substratum are essential to maintain and direct in-plane tissue growth (8, 9). When divisions have no favored orientation, growth is isotropic, whereas orientation along one specific axis can lead to tissue elongation (10, 11). As a consequence, the cues and mechanisms regulating the orientation of cell division have been the focus of much research.

Mitotic spindles in both isolated cells and tissues can alter their orientation in response to a variety of cues. Depending on the experimental conditions, spindle orientation can be influenced by cell shape, junctional cues, signals from the extracellular matrix, the stress field, or a combination of these cues (6, 12–21). To probe the cellular-scale response to tissue deformation, studies in vivo and in vitro have applied uniaxial deformation to isolated cells as well as epithelia and shown cell division to be oriented along the stretch axis (6, 17, 22, 23). Outside of a tissue context, elongated metaphase cells that are subjected to a uniaxial stretch perpendicular to their long axis reorient their spindle to a position intermediate between the directions provided by the shape and stress cues (17). In developing tissues, such as the zebrafish enveloping layer, a stress field applied perpendicular to the spindle axis causes reorientation (14). Collectively, these studies indicate that spindles can respond to externally applied deformation and stresses. However, how tissue–scale deformation impacts the tension distribution in the cortex of a mitotic cell is unclear. Moreover, whether and how spindles are able to respond to tension inhomogeneities within the actin cortex remains unknown. Indeed, the reorientation of spindles could arise from the activation of mechanosensitive signaling pathways or could emerge from changes in the balance of forces exerted by the spindle positioning apparatus.

To address the role of the mitotic cortex in spindle orientation, we used optogenetic activators of contractility to generate inhomogeneous tension within the cortex of mitotic cells and investigated the spindle response. Remarkably, an increase in cortical myosin and tension, specifically at cell poles, resulted in the reorientation of the metaphase spindle away from these regions, subsequently affecting the orientation of cell division. Spindle rotation arises due to a local reduction of the pulling forces exerted by cortical regulators on astral microtubules. Experiments and mathematical modeling suggest that rotation emerges from the interaction between the spindle positioning machinery and the cell

Author contributions: M.K., G.S., and G.C. designed research; M.K. and P.B. performed research; M.B.S., A.L., L.V., and E.F. contributed new reagents/analytic tools; M.K., P.B., and V.S. analyzed data; G.S. developed the model; and M.K., B.B., G.S., and G.C. wrote the paper.

The authors declare no competing interest.

This article is a PNAS Direct Submission.

[1]To whom correspondence may be addressed. Email: m.kelkar@ucl.ac.uk, guillaume.salbreux@unige.ch, or g.charras@ucl.ac.uk.

This article contains supporting information online at http://www.pnas.org/lookup/suppl/doi:10.1073/pnas.2121868119/-/DCSupplemental.

Published June 21, 2022.

cortex. Our data therefore suggest that mitotic spindles can respond to inhomogeneities in myosin activity and cortical tension to orient division away from regions of high tension.

Results

Increase in Cortical RhoA Activity Increases Cortical Tension. The tension distribution that arises in the cortex of mitotic cells in response to the application of a stress field remains poorly understood. However, the application of uniaxial stress to rounded mitotic cells likely leads to inhomogeneous tension in the cortex. To investigate the response of mitotic spindles to such tension inhomogeneities, we modulated cortical tension in mitotic cells by regulating the activity of RhoA at the plasma membrane using optogenetics. To this end, we used a previously established light-gated CRY2/CIBN dimerization system (24, 25). In this actuator, the DH-PH domain of a RhoA-specific GEF, p115-RhoGEF/Arhgef1 (26), is fused to CRY2-mCherry and stably expressed in MDCK cells alongside CIBN-GFP, which is targeted to the plasma membrane with a CAAX domain (Fig. 1*A*). Exposure to blue light induces a conformational change in CRY2, causing it to bind CIBN and relocalize the DH-PH domain to the plasma membrane (Fig. 1*A*). With this system, recruitment to the membrane can be restricted to subcellular regions as small as 5 μm (27) and optogenetic relocalization of GEF DH-PH to the membrane increases RhoA activity (25). We reasoned that RhoA activation should lead to an increase in myosin contractility and subsequently an increase in cortical tension. To verify this line of reasoning, we measured cortical tension in both interphase and mitotic rounded cells before and after exposure of the whole cell to blue light using atomic force microscopy (AFM) (*SI Appendix*, Fig. S1*A*). These measurements revealed a twofold (∼100%) increase in tension following optogenetic activation in interphase cells (Fig. 1 *B* and *C* and *SI Appendix*, Fig. S1*B*) and a ∼31% increase in mitotic cells (*SI Appendix*, Fig. S1*B*). The smaller increase observed in mitotic cells might arise because ∼twofold more myosin is localized to the cortex in mitosis (28), leading to a ∼twofold larger cortical tension than in interphase cells (29). These experiments confirm that GEF DH-PH relocalization modulates cortical tension in both interphase and in mitosis.

Next, we determined whether local accumulation of GEF DH-PH translated into a local increase in cortical tension. Cell shape is controlled by cortical tension, which depends strongly on myosin contractility (30). Therefore, we reasoned that changes in cell shape, in response to localized optogenetic activation, should indicate a change in cortical tension. To this end, we illuminated specific regions in MDCK cells synchronized in metaphase with brief pulses of a 473 nm blue laser every 2 min to maintain a constant level of CRY2, and therefore GEF DH-PH, at the membrane (*SI Appendix*, Fig. S1*C*). Optogenetic relocalization of DH-PH to both poles led to a decrease in the length of the polar axis (P) and an increase in the length of the equatorial axis (E), causing a small (∼3%) but significant reduction in the P/E ratio (*SI Appendix*, Fig. S1*E*) and flattening of the cell at the poles, which is indicative of a localized increase in tension. Along with AFM measurements showing an increase in cortical tension in response to global activation (Fig. 1 *B* and *C* and *SI Appendix*, Fig. S1*B*), these data indicate that localized optogenetic activation locally increases cortical tension.

Mitotic Spindle Orientation Responds to Local Differences in Cortical Tension Induced by RhoA Activation. To investigate the response of mitotic spindles to local inhomogeneities in cortical tension, we targeted our optogenetic actuator either to cell poles alone (bipolar), the equator alone (equatorial), or isotropically along the whole cell cortex (global) and examined the spindle response until the onset of cytokinesis. Because spindle orientation is strongly influenced by cell shape cues (31–33), we focused our experiments on quasi-spherical cells with a P/E ratio between 0.85 and 1.25 (mean ± SD = 1.06 ± 0.08) to investigate spindle response to changes in cortical tension with minimal contribution from shape cues (*SI Appendix*, Fig. S1*D*). Localized activation in small square regions (0.62 μm × 0.62 μm) specifically at cell poles (bipolar) led to a ∼20% increase in GEF accumulation in those regions without significantly affecting GEF levels at the equator (Fig. 1 *F* and *G* and *SI Appendix*, Fig. S2*F*). Remarkably, this resulted in an average ∼35° rotation of the mitotic spindle away from its original orientation, subsequently causing a change in the division axis in these cells (Fig. 1 *F* and *J*). Because spindle reorientation upon bipolar activation could be influenced by changes in cell shape, we characterized the correlation between cell shape and spindle rotation angle. We found no correlation between the final spindle rotation angle and the P/E ratio measured preactivation, 2 min postactivation, or at the first frame of spindle rotation (*SI Appendix*, Fig. S1*F*). In addition, we did not find a significant correlation between the final spindle rotation angle and the percentage shape change induced by optogenetic activation (*SI Appendix*, Fig. S1*G*). These analyses suggest that under our experimental conditions focusing on quasi-spherical cells, shape change does not appear to control spindle reorientation.

Spindle reorientation was specific to GEF relocalization, as it was not observed in cells expressing CRY2-mCherry without the DH-PH domain (control) (Fig. 1 *D*, *E*, and *J* and *SI Appendix*, Fig. S2*C*). Following this observation, we asked whether any spatial heterogeneity or temporal change in RhoA activity and cortical tension was sufficient to cause spindle reorientation. Although localized optogenetic activation at the equator (equatorial) (*SI Appendix*, Fig. S2*A*) or whole-cell optogenetic activation (global) (Fig. 1*H*) both led to GEF accumulation in those regions (*SI Appendix*, Fig. S2 *B*, *D*, and *E* and Fig. 1*I*), neither perturbed the average spindle orientation or the division axis (Fig. 1*J* and *SI Appendix*, Fig. S2*G*). Furthermore, spindle rotation only occurred in metaphase (Fig. 1*J*) with very little change in orientation from anaphase until cytokinesis (*SI Appendix*, Fig. S2*H*), suggesting that this phenomenon may be specific to metaphase. Consistent with this observation, when we carried out optogenetic activation at the poles in early anaphase, no spindle rotation was observed, indicating that rotation was no longer possible after anaphase onset (*SI Appendix*, Fig. S2*J*). Thus, our data show that the spindles specifically respond to a local increase in RhoA activity and cortical tension at cell poles during metaphase.

Following these observations, we sought to further characterize the spindle response to optogenetic activation in metaphase. In principle, the final angle that a spindle reaches should be influenced by its rotation speed and/or the time available for rotation until anaphase onset. The former proved to be the case as the speed of spindle rotation, measured from optogenetic activation until anaphase onset, was significantly higher in cells subjected to bipolar activation than in those under control condition (Fig. 1*K*). Moreover, optogenetic activation of the GEF at the cell poles did not lead to a significant difference in the time until anaphase onset (*SI Appendix*, Fig. S2*I*). Next, we measured the temporal evolution of the spindle position by plotting the spindle angle trajectories averaged over all cells up to 13 min postactivation. Here, we did not identify a significant difference in the final spindle position between control and bipolar activation conditions (*SI Appendix*, Fig. S2*K*). Because the time until anaphase onset upon bipolar GEF activation was more variable than in control cells (*SI Appendix*,

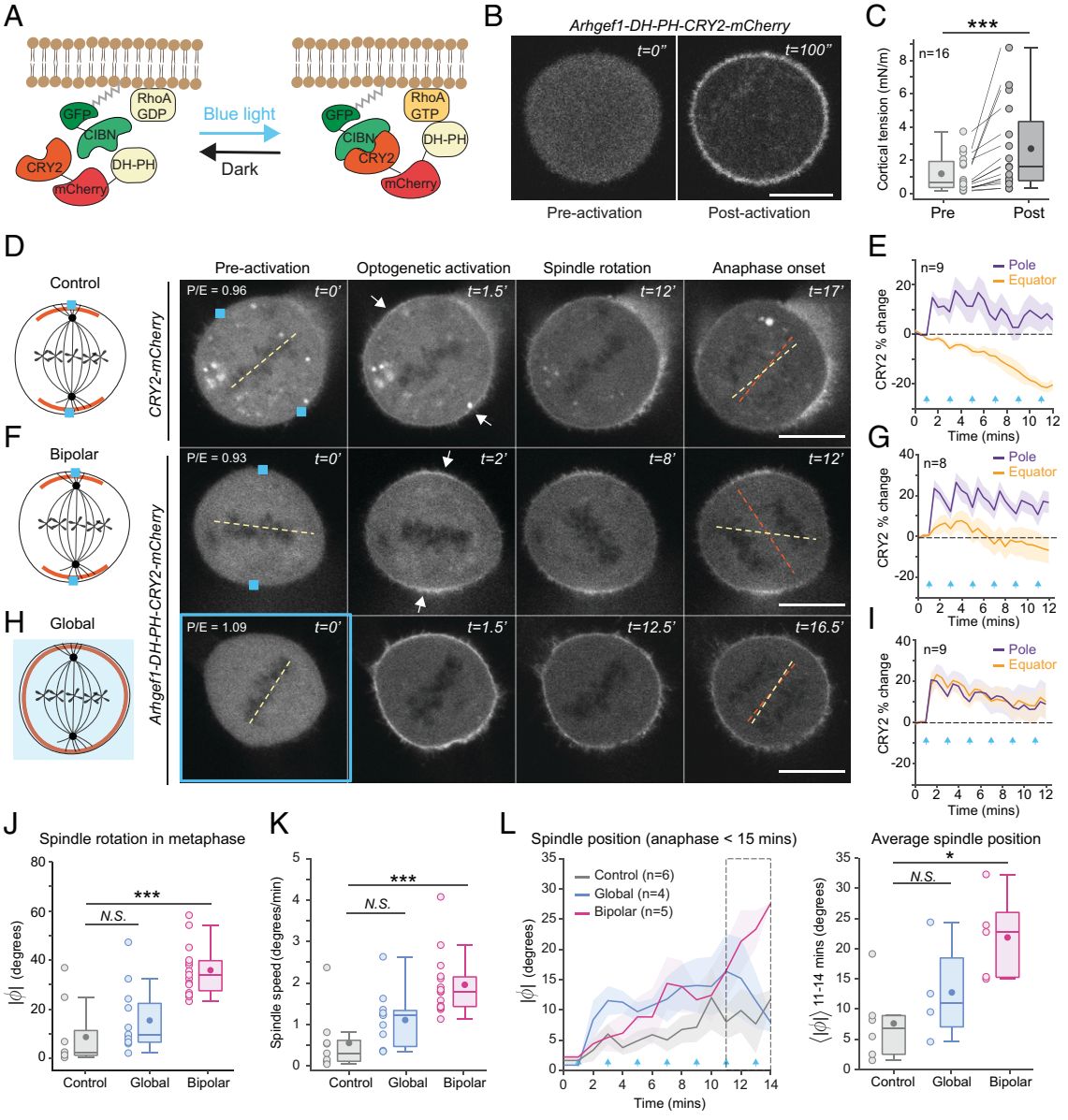

Fig. 1. Mitotic spindle orientation responds to inhomogeneities in RhoA activity and cortical tension (*A*) Schematic depicting the light-gated CRY2/CIBN dimerization system used to regulate RhoA activity. CIBN is fused to GFP and targeted to the plasma membrane using a CAAX motif. CRY2 is cytosolic, tagged with mCherry and fused to the DH-PH domain of a RhoA-specific GEF- Arhgef1/p115Rho-GEF. Upon illumination with 473 nm blue light, CRY2 undergoes a conformational change and binds to CIBN, thereby relocating the DH-PH domain of the GEF to the plasma membrane where it can activate RhoA. After illumination is stopped, CRY2 undergoes a slow detachment from CIBN and returns to the cytosol. (*B*) Representative confocal images of rounded interphase MDCK cells coexpressing CIBN-GFP-CAAX and Arhgef1-GEF-DH-PH-CRY2-mCherry viewed in the mCherry channel at t = 0 (preactivation) and t = 100 s after blue light illumination (postactivation). Time is in seconds. (*C*) Box plot showing cortical tension in interphase cells measured by AFM pre- and postexposure to blue light (n = 16 cells). Wilcoxon signed rank test; ***$P = 4.37 \times 10^{-4}$. (*D*) *Left*, Schematic showing the localization of CRY2-mCherry (red), after bipolar optogenetic activation in metaphase cells. *Right*, Time series showing localization of CRY2-mCherry in cells before and after bipolar optogenetic activation until anaphase onset. Time is in minutes. The preactivation P/E ratio is 0.96. (*E*) Temporal plot showing the percentage change in CRY2-mCherry intensity at the poles and equator after bipolar activation. Plot shows mean ± SEM (n = 9 cells). Blue arrows indicate the times of blue light stimulation. (*F*) *Left*, Schematic showing the localization of Arhgef1-DH-PH-CRY2-mCherry (red) after bipolar optogenetic activation in metaphase cells. *Right*, Time series showing localization of GEF-DH-PH-CRY2-mCherry in cells before and after bipolar optogenetic activation until anaphase onset. Time is in minutes. The preactivation P/E ratio is 0.93. (*G*) Temporal plot showing the percentage change in Arhgef1-DH-PH-CRY2-mCherry intensity at the poles and equator after bipolar activation. Plot shows mean ± SEM (n = 8 cells). Blue arrows indicate the times of blue light stimulation. (*H*) *Left*, Schematic showing the localization of Arhgef1-DH-PH-CRY2-mCherry (red) after global optogenetic activation in metaphase cells. *Right*, Time series showing localization of GEF-DH-PH-CRY2-mCherry in cells before and after global activation until anaphase onset. Time is in minutes. The preactivation P/E ratio is 1.09. (*I*) Temporal plot showing the percentage change in Arhgef1-DH-PH-CRY2-mCherry intensity at the poles and equator after global activation. Plot shows mean ± SEM (n = 9 cells). Blue arrows indicate the times of blue light stimulation. (*J*) Box plot showing spindle rotation angle in metaphase for cells under control (n = 9), global (n = 12), and bipolar (n = 15) activation. Angle is measured at anaphase onset relative to the preactivation orientation. Kruskal–Wallis and posthoc Dunn's test; Control vs. Bipolar: ***P = 0.0002; Control vs. Global: P = 0.4239 (N.S.). (*K*) Box plot showing spindle rotation speed after activation until anaphase onset for cells under control (n = 9), global (n = 11), and bipolar (n = 15) activation. ANOVA and Tukey–Kramer test; Control vs. Bipolar: ***P = 0.0002; Control vs. Global: P = 0.21 (N.S.). (*L*) *Left*, Trajectories of absolute spindle angles before and for 13 min after optogenetic activation for a subset of cells, whose anaphase occurs within 15 min of activation. Blue arrows indicate the times of blue light stimulation. *Right*, Box plot showing an average of the absolute spindle angle between 11 and 14 min. Control (n = 6), bipolar (n = 5), global (n = 4). ANOVA and Tukey–Kramer test; Control vs. Bipolar: *P = 0.017; Control vs. Global: P = 0.527 (N.S.). In panels *D*, *F*, and *H*, yellow and orange dashed lines indicate the position of the DNA in the metaphase plate before activation and at anaphase onset, respectively. Blue squares indicate the region of activation. White arrows point to regions of CRY2-mCherry or Arhgef1-DH-PH-CRY2-mCherry accumulation (Scale bars, 10 μm). Box plots show the median (dark line), interquartile range, mean (dark filled circle), and individual data points (light filled circle).

Fig. S2*I*), we instead decided to analyze the temporal evolution of spindle position in a subset of cells that enter anaphase within 15 min of optogenetic activation. Again, in this case, spindles underwent a greater rotation following bipolar GEF activation than under the control condition (Fig. 1*L*). Finally, we plotted all of our spindle angle trajectories by aligning them to the onset of anaphase, rather than to the start of the optogenetic stimulus. Here, we observed a significant difference in the average spindle position upon bipolar GEF activation (*SI Appendix*, Fig. S2*L*).

Taken together, these results demonstrate that the increased levels of RhoA activity and cortical tension induced by the local recruitment of GEF DH-PH to cell poles increase the rotation speed of the spindle to reorient divisions.

Mitotic Spindles Rotate Away from Myosin-Enriched, Tensed Cortical Regions. Next, we investigated the molecular changes in the cortex leading to spindle rotation. We first verified that localized optogenetic actuation of GEF DH-PH indeed led to local activation of RhoA by imaging the RhoA biosensor iRFP-AHDPH (34). Bipolar activation led to a ∼15% increase in RhoA biosensor intensity at the poles without significantly affecting equatorial levels (*SI Appendix*, Fig. S3*A*). RhoA activates Rho-associated coiled-coiled kinase (ROCK) (35), which increases myosin activity through two pathways: phosphorylating and activating the regulatory light chain of myosin-II while simultaneously inhibiting myosin phosphatase (36, 37). RhoA also acts on the F-actin scaffold directly by activation of the cortical actin nucleator mDia1 (38, 39) and indirectly via ROCK, which has been shown to inactivate cofilin via phosphorylation through LIM-kinase (40). Thus, a change in RhoA activity can potentially regulate cortical tension by activating myosins and/or by changing the F-actin scaffold.

To determine how RhoA increased cortical tension, we examined the response of cortical myosin and F-actin to the optogenetic actuation of GEF DH-PH. Bipolar activation led to an increase in MRLC-iRFP intensity at cell poles, which reached a steady value within ∼3 min of activation (2.8 ± 0.74 min, $n = 8$ cells), marking it as a potential early event that preceded spindle rotation away from the poles (Fig. 2*A*). Consistent with GEF relocalization (Fig. 1*G*), we observed a significant ∼15% increase in myosin intensity at the poles but no significant changes in the future pole or at the equator (Fig. 2 *B*–*D*). In contrast, F-actin levels imaged using LifeAct-iRFP displayed no clear changes in intensity (*SI Appendix*, Fig. S3*B*). Thus, these data indicate that local activation of RhoA leads to local differences in myosin levels in the cortex that underlie inhomogeneities in cortical tension.

To determine the role of myosin-generated cortical tension in spindle rotation, we performed optogenetic activation experiments in the presence of inhibitors of myosin activity (Fig. 2*E*). Inactivation of Rho-kinase using Y-27632 or direct inhibition of myosin activity using photostable s-nitro-blebbistatin (41) abolished spindle rotation, signifying that myosin activity at the poles is essential to enable spindle rotation (Fig. 2*F*). As both treatments decrease cortical tension (29, 42) and do not disrupt spindle organization (*SI Appendix*, Fig. S4*D*), spindles may therefore be sensitive either to myosin activity directly or to the increase in cortical tension that it causes.

Taken together, our results suggest that localized RhoA activation at the poles acts through a local increase in myosin enrichment and cortical tension to induce spindle rotation.

Spindle Rotation Depends on Cortical Localization of NuMA and Pulling Forces Exerted by Dynein. We next investigated the role of the previously identified spindle positioning machinery in driving rotation. Mitotic spindle positioning depends on a conserved complex of Gαi, LGN, and NuMA localized at the plasma membrane that recruits the microtubule minus–end directed motor protein dynein (8, 43, 44) (Fig. 3*A*). Astral microtubules that extend from the spindle poles to the cortex play a key role in spindle positioning by exerting pushing forces on the cortex generated by microtubule growth and pulling forces that are associated with a combination of microtubule shrinkage and dynein motor activity (45–48). To investigate the contribution of these proteins to spindle rotation, we performed inactivation experiments to block each component in turn. Inhibition of dynein activity using Ciliobrevin D (49) led to spindle collapse in 21% of cells upon bipolar optogenetic activation. However, in the cells that successfully divided, spindle rotation was abolished (Fig. 3*B*), indicating that dynein-mediated pulling forces are essential. In control metaphase cells, NuMA is enriched at the cell poles and depleted at the cell equator (*SI Appendix*, Fig. S4*A*). Therefore, we tested the importance of NuMA for spindle rotation by reducing its cortical levels using low doses of MLN-8237. This treatment results in partial inhibition of the activity of aurora-A kinase, which led to the relocalization of NuMA from the cortex to the spindle pole (50) (*SI Appendix*, Fig. S4*A*). Treatment with MLN-8237 blocked spindle rotation (Fig. 3*B*). This demonstrated an essential role for cortical NuMA for spindle rotation in response to bipolar GEF DH-PH activation. Because these inhibitors may also affect other processes in the cell, we verified that they did not alter astral microtubule length or levels of phosphorylated myosin at the cortex (*SI Appendix*, Fig. S4 *B* and *D*). Finally, depolymerization of astral microtubules using low doses of nocodazole (*SI Appendix*, Fig. S4*C*) also prevented spindle rotation (Fig. 3*B*), indicating that forces exerted by astral microtubules are essential for spindle rotation. Together, these experiments indicate that cortical regulators and astral microtubules participate in spindle rotation in response to bipolar GEF activation.

We considered two possible mechanisms by which cortical regulators and astral microtubules could affect spindle rotation. First, changes in cortical tension following bipolar activation of GEF DH-PH may affect the localization or enrichment of cortical regulators via mechanotransduction; second, spindle rotation may arise from a change in the balance of forces exerted on astral microtubules. Recent work has shown that optogenetic cortical targeting of NuMA in human cells is sufficient to recruit the dynein–dynactin complex and account for efficient spindle positioning (51). Therefore, a change in the distribution of NuMA would lead to localized changes in the forces applied on astral microtubules and cause spindle rotation. To test this hypothesis, we imaged the localization of iRFP-NuMA upon optogenetic activation. We observed no significant change in the intensity of NuMA at both the pole and the equator, while the future pole showed a small decrease in intensity over 14 min post bipolar activation (Fig. 3 *C*–*E*). To verify that NuMA remains polarized both before and after optogenetic activation, we measured the ratio of pole to equator (P/E) and future pole to equator (FP/E) NuMA fluorescence over time. This ratio remained significantly above 1.0 over 14 min post activation (Fig. 3*F*). Finally, to examine whether the pattern of NuMA changed prior to spindle rotation, we aligned the intensity traces to the frame where the spindle begins to rotate and observed no significant changes in NuMA levels at the pole, equator, or future pole over time (*SI Appendix*, Fig. S4*E*), with NuMA remaining polarized prior to spindle rotation (*SI Appendix*, Fig. S4*F*). These data indicate that the enrichment of NuMA at the poles, contributing to pulling force generation, is not perturbed postactivation. Moreover, the localization and intensity of NuMA does not change prior to spindle rotation.

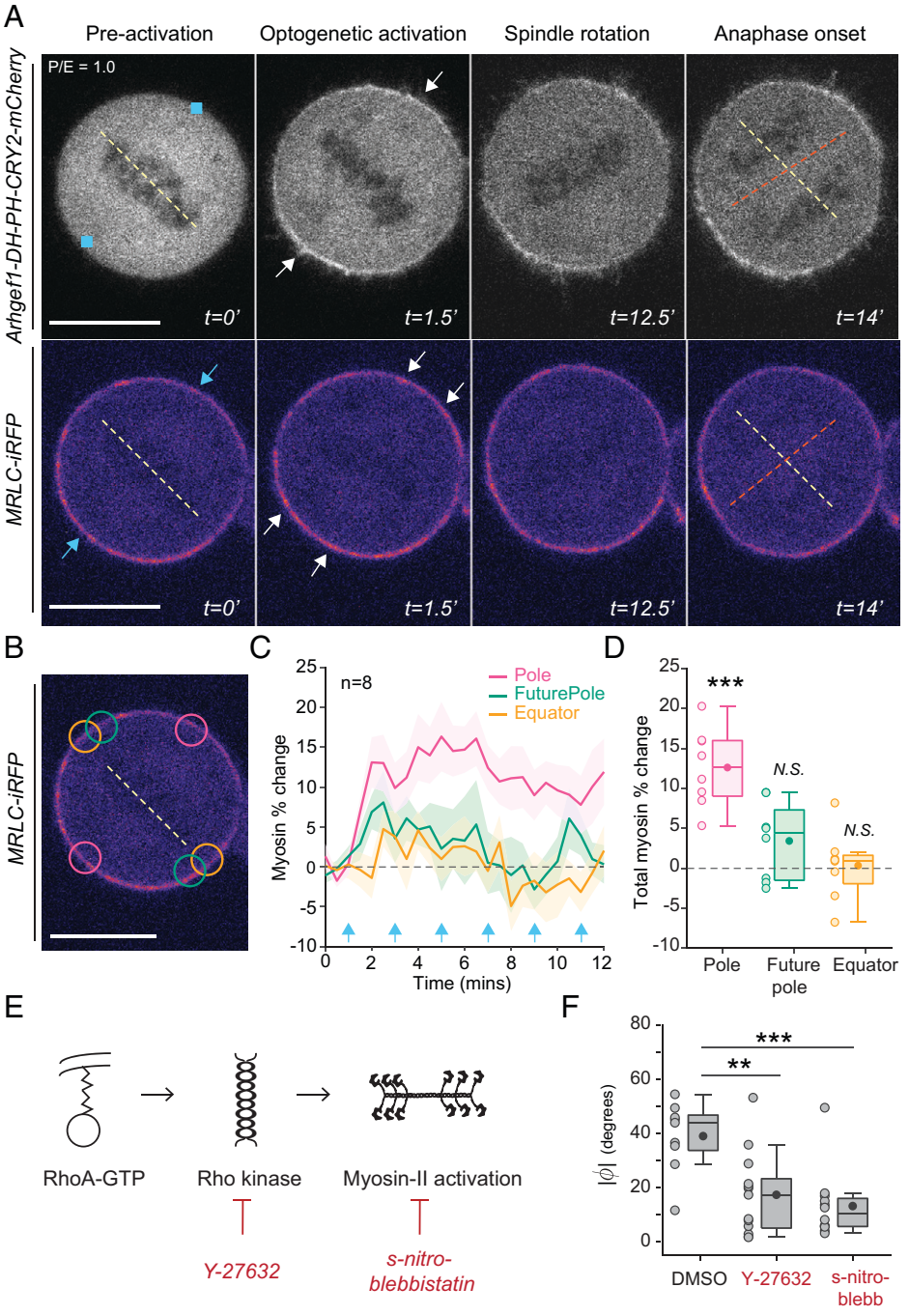

Fig. 2. Mitotic spindles rotate away from myosin-enriched tensed cortical regions. (*A*) *Top*, Time series showing localization of Arhgef1-DH-PH-CRY2-mCherry in cells before and after bipolar optogenetic activation until anaphase onset. *Bottom*, Time series showing the corresponding localization of MRLC-iRFP with low intensities appearing in black and high intensities in magenta. Yellow and orange dashed lines indicate the position of the DNA in the metaphase plate before activation and at anaphase onset, respectively. Blue squares (*Top*) and blue arrows (*Bottom*) indicate the region of activation. White arrows point to regions of GEF-DH-PH accumulation (*Top*) and myosin accumulation (*Bottom*) (Scale bar, 10 μm). Time is in minutes. The preactivation P/E ratio is 1.0. (*B*) MRLC-iRFP image at t = 0 as in *A* (*Bottom*) showing the regions used to measure fluorescence intensities in (*C* and *D*), with pole in pink, future pole in green, and equator in yellow (Scale bar, 10 μm). (*C*) Temporal plot showing the percentage change in MRLC-iRFP intensity at the pole, future pole, and equator after bipolar activation. Plot shows mean ± SEM (n = 8 cells). Blue arrows indicate the times of blue light stimulation. (*D*) Box plot showing the total percentage change in MRLC-iRFP intensity between 1 and 12 min at the pole, future pole, and equator for cells shown in *C* (n = 8 cells). Student's t test compared with 0% change; Pole: ***$P = 1.5 \times 10^{-4}$; Future pole: $P = 0.0840$ (N.S.); Equator $P = 0.8247$ (N.S.). (*E*) Schematic depicting part of the signaling downstream of RhoA. Active RhoA-GTP activates Rho-kinase that in turn activates myosin-II by direct phosphorylation and indirectly by inhibition of myosin phosphatase. Y-27632 and s-nitro-blebbistatin block myosin contractility by inhibiting Rho-kinase and myosin ATPase activity, respectively. (*F*) Box plot showing spindle rotation angle in metaphase for control cells treated with DMSO (n = 9), 50 μM Y-27632 (n = 13), and 20 μM s-nitro-blebbistatin (n = 12), respectively. Angle is measured at anaphase onset relative to the preactivation orientation. ANOVA and Tukey–Kramer test; DMSO vs. s-nitro-blebbistatin: ***P = 0.0005; DMSO vs. Y-27632: **P = 0.0028. Box plots show the median (dark line), interquartile range, mean (dark filled circle), and individual data points (light filled circle).

Taken together, our data suggest that spindle reorientation in response to bipolar GEF activation does not occur due to a change in the localization of cortical regulators. Instead, the spindle may reorient in response to changes in the cortex itself.

Spindle Rotation Results from a Local Decrease in Pulling Force Exerted on Astral Microtubules at Regions of High Cortical Tension. To investigate our second hypothesis, we tested whether spindle rotation arises from a change in the balance of forces exerted on astral microtubules upon GEF DH-PH activation. First, we confirmed that metaphase spindles are subjected to a tensile force due to the interaction of astral microtubules with the cortex (52). To this end, we severed astral microtubules at one spindle pole using laser ablation and imaged changes in the centrosome position. The rapid inward movement of the centrosome after ablation indicated that the centrosomes are subjected to a net pulling force (*SI Appendix*, Fig. S5 *A* and *B*).

Having established the resultant of the forces acting on the centrosomes in control conditions, we monitored the displacement of the centrosomes in response to optogenetic activation. We reasoned that a displacement of the centrosome toward the cell center would occur following a reduction in the cortical pulling forces and/or as a result of an increase in the microtubule pushing forces, while displacement away from the cell center would suggest an increase in the pulling forces and/or a decrease in the pushing forces (Fig. 4*A*). First, we carried out optogenetic activation at only one pole (unipolar). This led to a displacement of the centrosome toward the cell center on the activated side (activated pole), whereas the centrosome on the nonactivated side (nonactivated pole) underwent little if any change in position (Fig. 4 *B* and *D*). Similarly,

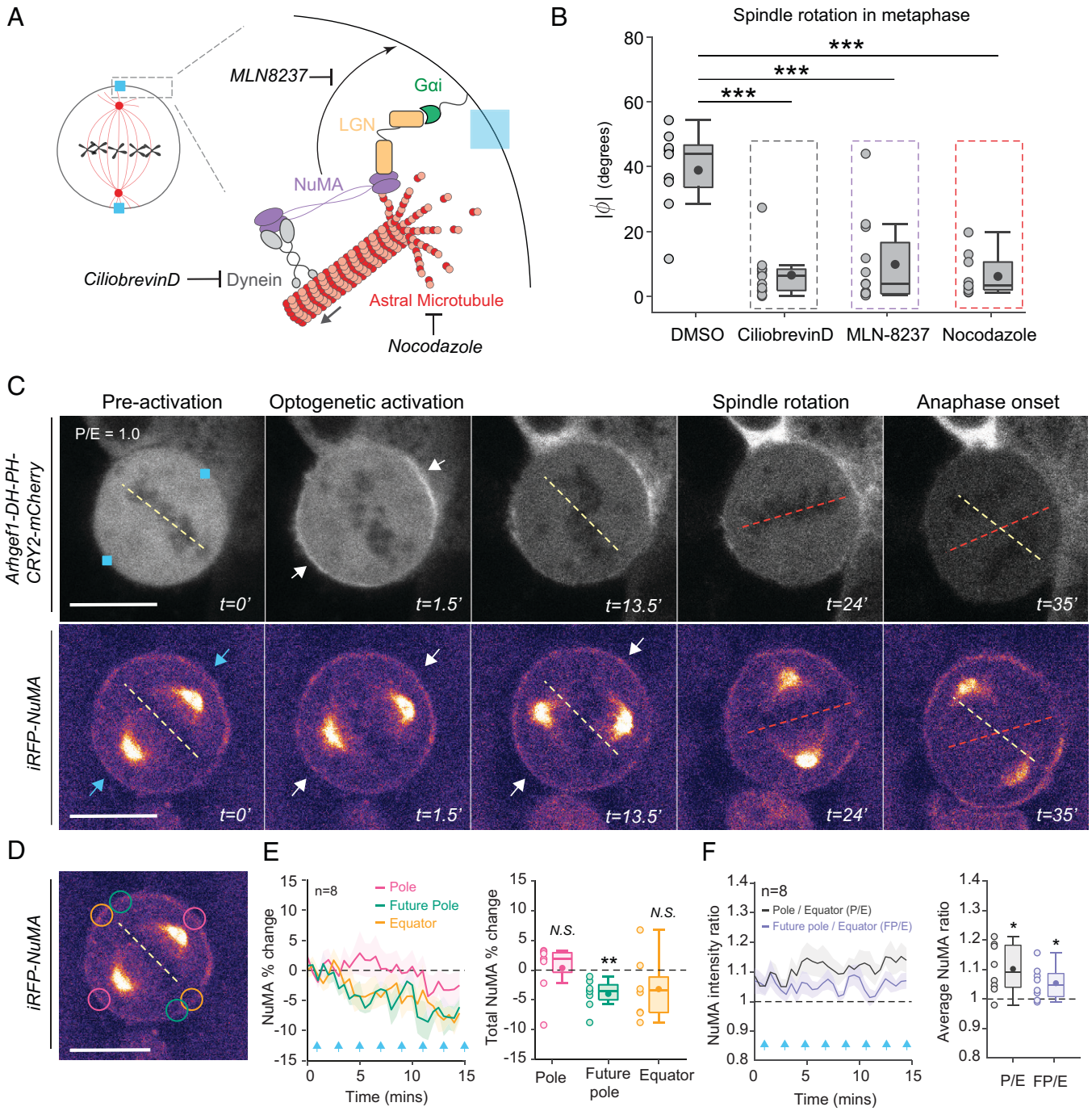

Fig. 3. Spindle rotation depends on cortical localization of NuMA and pulling forces exerted by dynein. (*A*) Schematic model showing cortical regulators involved in spindle positioning. The ternary complex of Gα*i*, LGN, and NuMA is anchored at the plasma membrane and recruits the motor protein dynein. Dynein exerts minus-end directed pulling forces on astral microtubules (gray arrow) to position the spindle. Ciliobrevin D blocks the ATPase activity of dynein and low doses of MLN-8237 partially inhibit aurora-A kinase, thus trapping NuMA at the spindle pole and blocking its transport to the cortex, and low doses of nocodazole block the polymerization of astral microtubules without severely affecting the spindle. (*B*) Box plot showing spindle rotation angle in metaphase for control cells treated with DMSO (n = 9), 10 μM Ciliobrevin D (n = 13), 100 nM MLN-8237 (n = 12), and 20 nM nocodazole (n = 10). Angle is measured at anaphase onset relative to the preactivation orientation. ANOVA and Tukey–Kramer test; DMSO vs. Ciliobrevin D: ***P < 0.001; DMSO vs. nocodazole: ***P < 0.001; DMSO vs. MLN-8237: ***P < 0.001. (*C*) *Top*: Time series showing localization of Arhgef1-DH-PH-CRY2-mCherry in cells before and after bipolar optogenetic activation until anaphase onset. *Bottom*, Time series showing the corresponding localization of iRFP-NuMA with low intensities appearing in black, medium intensities in magenta, and high intensities at the spindle poles in yellow. Yellow and orange dashed lines indicate the position of the DNA in the metaphase plate before activation and at anaphase onset, respectively. Blue squares (*Top*) and blue arrows (*Bottom*) indicate the region of activation. White arrows point to regions of GEF-DH-PH accumulation (*Top*) and NuMA (*Bottom*) (Scale bar, 10 μm). Time is in minutes. The preactivation P/E ratio is 1.0. (*D*) iRFP-NuMA image at t = 0 as in *C* (*Bottom*) showing the regions used to measure fluorescence intensity in *E*, with pole in pink, future pole in green, and equator in yellow (Scale bar, 10 μm). (*E*) *Left*, Temporal plot showing the percentage change in iRFP-NuMA intensity at the pole, future pole, and equator after bipolar activation. Plot shows mean ± SEM (n = 8 cells). Blue arrows indicate the times of blue light stimulation. *Right*, Box plot showing the total percentage change in iRFP-NuMA intensity between 1 and 15 min at the pole, future pole, and equator for cells shown in *E* (*Left*). Student's t test compared with 0% change; Pole: P = 0.8162 (N.S.); Future pole: **P = 0.0023; Equator: P = 0.1162 (N.S.). (*F*) *Left*, Temporal plot showing the P/E ratio and (FP/E) ratio of NuMA for cells shown in *E*. *Right*, Box plot showing the average NuMA intensity ratios of individual cells. Student's t test compared with a ratio of 1; P/E: *P = 0.011; FP/E: *P = 0.03. Box plots show median (dark line), interquartile range, mean (dark filled circle), and individual data points (light filled circle).

following bipolar activation, we observed an inward displacement of both centrosomes (Fig. 4 *C*, *Top*, and *E*). These results suggest that optogenetic activation leads to either a reduction in the pulling force exerted by dynein or to an increase in the pushing force exerted by astral microtubules in myosin-enriched tensed cortical regions.

To distinguish between these scenarios, we measured centrosome displacement in cells treated with MLN-8237 that had reduced levels of cortical NuMA and therefore less cortical dynein (*SI Appendix*, Fig. S4*A*) (50). We reasoned that if optogenetic activation increases the pushing force, then we should still observe centrosome displacement in MLN-8237–treated cells, whereas if optogenetic activation reduces the pulling force, then we should observe little or no centrosome displacement. Treatment with MLN-8237 abolished the inward displacement of the centrosomes (Fig. 4 *C*, *Bottom*, and *E*). Our data therefore suggest that localized changes in myosin abundance and cortical tension following bipolar GEF activation lead to a local reduction in the pulling force exerted on astral microtubules, resulting in centrosome displacement towards the cell center. We hypothesize that it is this change in the balance of forces acting on the astral microtubules that enables spindle rotation.

Spindle Rotation is an Emergent Property of the Molecular Mechanisms of Force Generation on Astral Microtubules. Under control conditions, the stable bipolar spindle orientation is established by forces exerted on astral microtubules by dynein motors, anchored to the plasma membrane by a complex comprising Gαi, LGN, and NuMA. To explore how these forces result in a stable spindle position and how this stable position responds to changes in cortical tension, we developed a simplified mathematical model of spindle positioning based on our experimental data and current knowledge of the forces exerted on spindles (*SI Appendix*, *Supplementary Theory*). We considered a circular mitotic cell of radius R with two centrosomes separated by a distance $2l_c$, from which astral microtubules emanated with a maximal length l_m (Fig. 5*A* and *SI Appendix*, Fig. S6 *A* and *B*). The spindle's orientation with respect to a horizontal reference axis was parameterized by an angle (ϕ), and the spindle was subjected to a torque (Γ) (Fig. 5*A* and *SI Appendix*, Fig. S6*A*). In line with previous work, Γ arose from dynein motors exerting forces acting at the tip of astral microtubules touching the cell cortex (33, 53–55). The distribution of pulling forces along the cortex was taken to be proportional to the experimentally measured NuMA fluorescence profile (*SI Appendix*, Fig. S4*A* and Fig. 5*B*). In the model, the cortical force distribution $f(\theta)$ was parameterized using a function of the form $f(\theta) = f_+^0 g_N(\theta)$, where f_+^0 has a dimension of a pulling force per microtubule and $g_N(\theta)$ is a periodic function whose shape was evaluated from the experimentally measured NuMA fluorescence profile along the cell periphery (*SI Appendix*, *Supplementary Theory*, Figs. S4*A* and S6*E* and Fig. 5*B*). With these data, our model computed a torque (Γ/Γ_0) acting on the spindle as a function of its angular position (ϕ). Under control conditions (Fig. 5*C*, control), when ϕ was positive the torque was negative, signifying that the spindle would move back toward the 0° orientation, and conversely, when ϕ was negative the torque was positive, again moving the spindle back toward 0°. Therefore, our model predicted that the 0° orientation is a stable position of the spindle under control conditions.

We next asked how the spindle position would change under a theoretical perturbation of the distribution of cortical forces. We found that when the spindle was subjected to an additional bipolar profile of cortical forces locally reducing the pulling force, the spindle could either keep its stable 0° orientation or leave its original position to move to a new stable orientation, depending on the magnitude of the perturbation (*SI Appendix*, Fig. S6 *F*–*H*). Next, we parameterized the cortical force distribution for our optogenetic activation experiments. Since the polar enrichment of NuMA does not change with optogenetic activation (Fig. 3 *C*–*F* and *SI Appendix*, Fig. S4 *E* and *F*), $g_N(\theta)$ was kept the same as in the control condition. In addition, the change in myosin distributions for both bipolar and global activation conditions was fitted with a periodic function (Fig. 5*B* and *SI Appendix*, Fig. S6 *C* and *E* and *Supplementary Theory*). The force distribution acting on the spindle was then computed by adding a new contribution to the force profile, now taking the form $f(\theta) = g_N(\theta)\,[f_+^0 - f_-^0 g_M(\theta)]$ (*SI Appendix*, *Supplementary Theory*), where $g_M(\theta)$ is proportional to the change in myosin intensity after activation. Here, based on our experiments, we assumed that the effect of myosin is to decrease cortical pulling forces on microtubules, with a magnitude that depends on both the NuMA and the myosin distributions. To simulate decreased pulling forces following activation, we chose values of the ratio f_-^0/f_+^0 that were sufficiently large but still low enough such that $f(\theta)>0$ (*SI Appendix*, Fig. S6*I*). Our model predicted a new stable spindle orientation for bipolar activation but no change for global activation, qualitatively consistent with our experiments (Fig. 5*C*, bipolar and global). Indeed, under bipolar activation conditions, when ϕ was small and positive the torque was positive, indicating that the spindle would move away from 0° toward a new, positive tilted orientation. Conversely, when ϕ was small and negative the torque was negative, indicating that the spindle moved away from 0° and toward a negative tilted orientation. Therefore, our model predicted that mitotic spindles move away from the 0° orientation to a new stable position in response to bipolar activation but not in response to global activation.

Next, we asked whether our simulation could capture the dynamics of rotation by using a dynamic model of spindle motion. Here, the spindle moved according to the torque acting on it, and its movement was resisted by an effective rotational friction force. Our experimental data indicated that even under control conditions, the spindle angle tends to fluctuate (*SI Appendix*, Fig. S6*D*). We modeled these fluctuations by introducing a random force acting on the spindle motion, leading to spindle diffusion with a diffusion constant D (*SI Appendix*, *Supplementary Theory*). Experimental measurements of the mean square rotational displacement of the spindle then allowed us to determine the diffusion constant D and a characteristic time $\bar{\tau}$ that depended on friction and on the pattern of cortical forces (*SI Appendix*, *Supplementary Theory* and Fig. S6*D*). Incorporating these experimental values into our model allowed us to predict the temporal evolution of the spindle orientations. The predicted time that the spindles needed to reach their stable orientation was a few minutes, although experimentally, the spindle did not appear to reach a stable state before anaphase onset (~15 min) (Figs. 1*L* and 5*D* and *SI Appendix*, Figs. S2*I* and S6 *J* and *K*).

Increasing the magnitude of the ratio f_-^0/f_+^0 led to spindle dynamics closer to those observed in experiments, where the spindle position did not saturate by 15 min (Fig. 1*L* and *SI Appendix*, Fig. S7*C*). In this case, the model predicted that both bipolar and global optogenetic activation would give rise to a new stable spindle orientation (*SI Appendix*, Fig. S7*A*). The kinetics of reorientation were slower, with spindles reaching their stable orientation only after ~40 min, much longer than the median time until anaphase onset in our experiments (~15 min, *SI Appendix*, Figs. S2*I* and S7 *E* and *F*). When we limited our predictions to durations of 12 min, bipolar activation gave rise to rotations consistent with those observed experimentally (*SI Appendix*, Fig. S7 *C* and *D*), whereas global

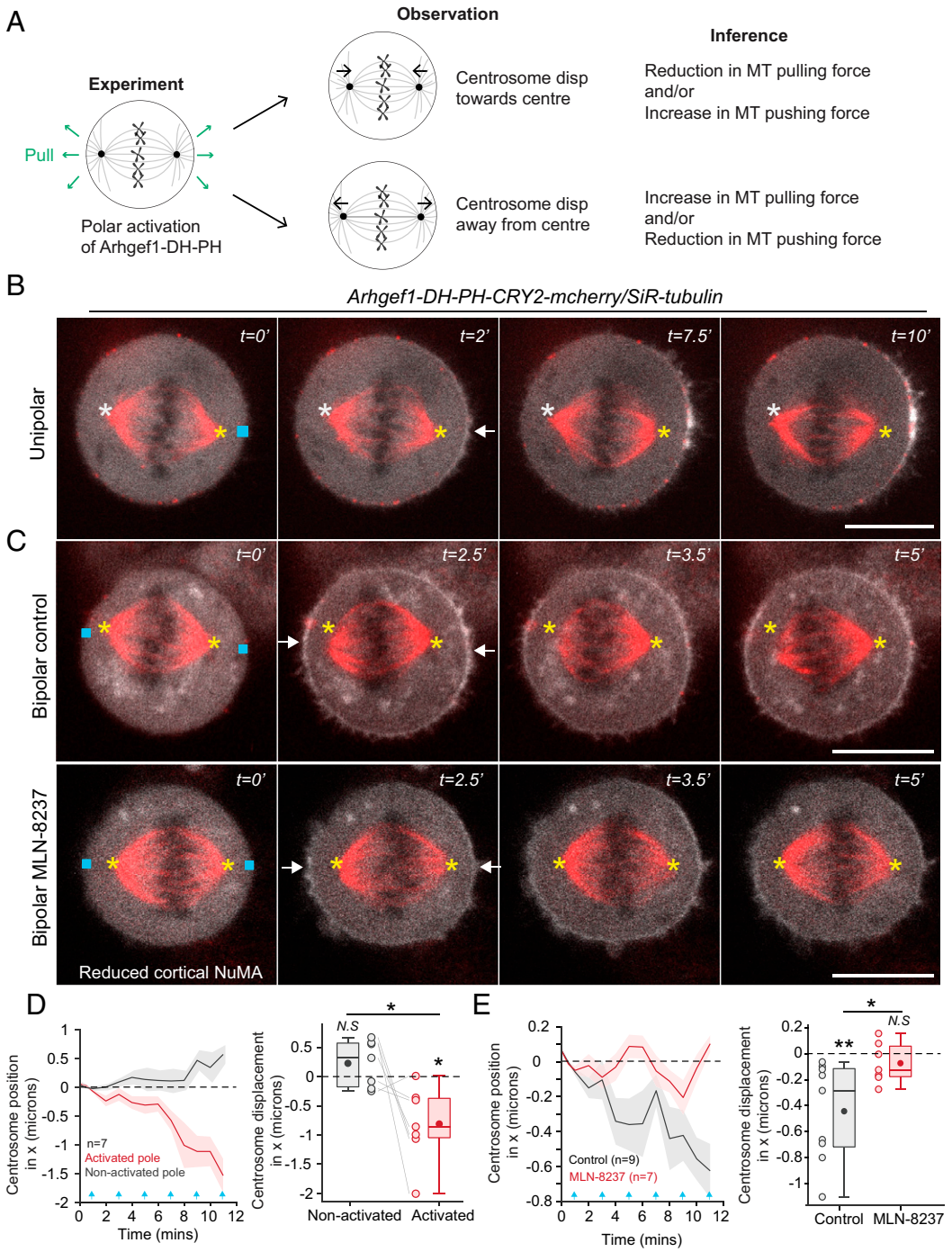

Fig. 4. Spindle rotation results from a local decrease in pulling force exerted on astral microtubules at regions of high cortical tension. (*A*) Schematic depicting the displacement of centrosomes as an indicator of forces acting on the spindle after polar optogenetic activation. An inward displacement of the centrosome toward the cell center (black arrows) could result from a reduction in pulling force and/or an increase in pushing force (*Top*). In contrast, an outward displacement of the centrosome away from the cell center (black arrows) would result from an increase in pulling force and/or a decrease in pushing force (*Bottom*). (*B*) Time series showing Arhgef1-DH-PH-CRY2-mCherry (gray) and siR-tubulin (red) in cells before and after unipolar optogenetic activation until anaphase onset. Blue square indicates the region of activation. White arrow points to the region of GEF-DH-PH accumulation. The positions of the two centrosomes at t = 0′ are marked with a yellow star (centrosome on the activated pole, AP) and a white star (centrosome on the nonactivated pole, NAP), respectively (Scale bar, 10 μm). Time is in minutes. (*C*) *Top*, Time series showing Arhgef1-DH-PH-CRY2-mCherry (gray) and siR-tubulin (red) in cells before and after bipolar optogenetic activation until anaphase onset. *Bottom*, Time series as shown in *Top*, in cells treated with MLN-8237. Blue squares indicate the regions of activation. White arrows point to the regions of GEF accumulation. The positions of the two centrosomes at t = 0′ are marked with yellow stars (Scale bar, 10 μm). Time is in minutes. (*D*) *Left*, Temporal plot showing the positions of the two centrosomes along the x-axis following unipolar optogenetic activation for cells shown in *B*. The displacement of each centrosome is measured with the convention that movement toward the cell center is negative and movement away from the center is positive. Plot shows mean ± SEM (n = 7 cells). Blue arrows indicate the times of blue light stimulation. *Right*, Box plot showing total centrosome displacement along the x-axis until 12 min. Student's t test compared with 0 μm displacement; NAP: P = 0.1813 (N.S.); AP: *P = 0.0169; paired Student's t test; NAP vs. AP: *P = 0.03. (*E*) *Left*, Temporal plot showing the position of the two centrosomes along the x-axis following bipolar optogenetic activation for control (n = 9) and MLN-8237 (n = 7) treated cells shown in *C*. The displacement of each centrosome is measured with the convention that movement toward the cell center is negative and movement away from the center is positive. Plot shows mean ± SEM. Blue arrows indicate the times of blue light stimulation. *Right*, Box plot showing total centrosome displacement along the x-axis until 12 min. Student's t test compared with 0 μm displacement; Control: **P = 0.0078; MLN-8237: P = 0.2518 (N.S.). Unpaired Student's t test; Control vs. MLN-8237: *P = 0.029. Box plots show median (dark line), interquartile range, mean (dark filled circle), and individual data points (light filled circle).

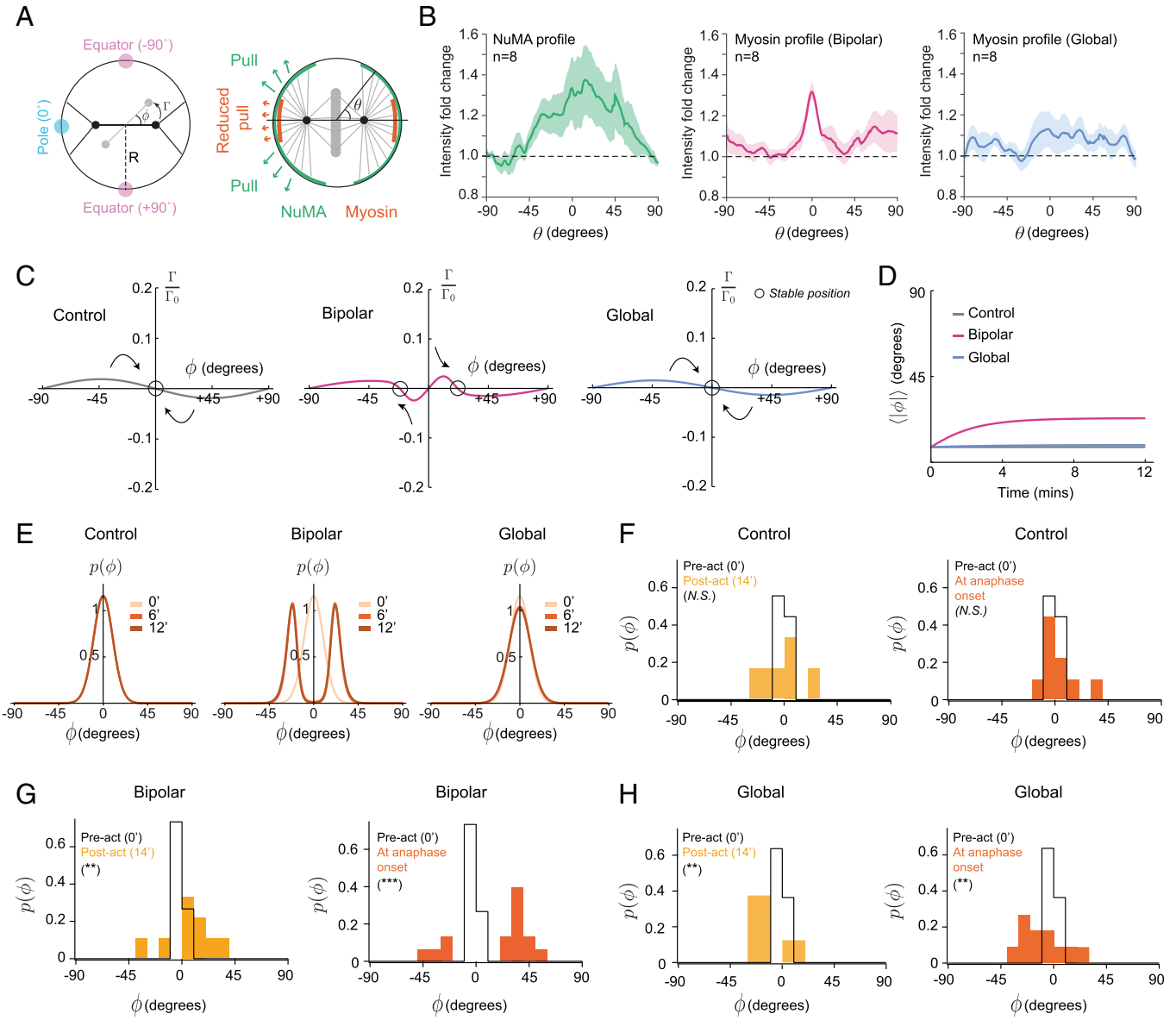

Fig. 5. Spindle rotation is an emergent property of the molecular mechanisms of force generation on astral microtubules. (*A*) *Left*, Schematic depicting the model of spindle positioning. We consider a circular cell of radius *R*. The spindle is depicted as a solid line linking two solid circles, which indicate the spindle poles. The reference spindle position is chosen to be horizontal and is shown in black. The spindle position at time t is shown in light gray. Astral microtubules emanate from the spindle poles with a uniform angular distribution and can contact the cortex if they are sufficiently long (solid black lines). At time t, the spindle makes an angle ϕ with the horizontal axis and is subjected to a torque Γ arising from cortical forces acting on astral microtubules. The spindle angle $\phi = 0$ corresponds to the spindle pointing toward the cell poles, while $\phi = \pm 90^\circ$ corresponds to the spindle pointing toward the equator. *Right*, Schematic showing the distribution of pulling forces at the cortex (green) as observed from the distribution of NuMA. θ denotes the polar angle of a point on the cell cortex. Astral microtubules are subjected to a pulling force when they interact with force generators at the cortex. In regions of optogenetic activation (red), they are subjected to a reduced pulling force. (*B*) *Left*, Normalized fluorescence intensity cortical profile of NuMA along the cell cortex as a function of the angle θ obtained from experimental immunostaining data of NuMA. The profile is normalized to the intensity at the equator ($n = 8$ cells). *Middle*, Spatial profile of fluorescence intensity of myosin along the cortex normalized to preactivation intensity after bipolar optogenetic activation ($n = 8$ cells). *Right*, Spatial profile of fluorescence intensity of myosin along the cortex normalized to preactivation intensity after global optogenetic activation ($n = 8$ cells). $\theta = 0$ represents the cell pole and $\theta = \pm 90^\circ$ represents the equator. Plots show mean ± SEM. (*C*) Predicted normalized torque (Γ/Γ_0) as a function of spindle angle (ϕ) for control (*Left*), bipolar (*Middle*), and global (*Right*) activation. Arrows indicate the direction of spindle rotation. Stable spindle positions are indicated by black circles. Profiles of cortical pulling forces and reduction in cortical pulling forces are taken proportional to the fluorescence intensity profile of NuMA and myosin, respectively, as shown in *B*. See *SI Appendix, Supplementary Theory* for further information. (*D*) Predicted average absolute value of the spindle angle as a function of time after optogenetic activation for different conditions. The spindle angle is measured between -90° and 90°, and the absolute value is averaged. (*E*) Predicted probability distribution of the spindle angle $p(\phi)$ at successive times (t = 0, 6, 12 mins) after optogenetic activation under control, bipolar, and global activation. (*F*) Histogram showing the experimental probability distribution of the spindle angles $p(\phi)$ plotted as a function of spindle angle (ϕ), preactivation and 14 min postactivation (*Left*) and preactivation and at anaphase onset (*Right*) for control cells. Two-sample Kolmogorov–Smirnov test; Control; preactivation vs. 14′ postactivation: $P = 0.23$ (N.S.); preactivation vs. anaphase onset: $P = 0.60$ (N.S.). Preactivation and anaphase onset ($n = 9$); 14′ postactivation ($n = 6$). (*G*) Histogram, as in *F*, for cells after bipolar activation. Two-sample Kolmogorov–Smirnov test, Bipolar; preactivation vs. 14′ postactivation: $^{**}P = 0.0065$; preactivation vs. anaphase onset: $^{***}P = 2.3 \times 10^{-4}$. Preactivation and anaphase onset ($n = 15$); 14′ postactivation ($n = 9$). (*H*) Histogram, as in *F*, for cells after global activation. Two-sample Kolmogorov–Smirnov test, Global; preactivation vs. 14′ postactivation: $^{**}P = 0.0046$; preactivation vs. anaphase onset: $^{**}P = 0.0025$. Preactivation and anaphase onset ($n = 11$); 14′ postactivation ($n = 8$).

activations only gave rise to small rotations because of the lower torques generated under this condition (*SI Appendix*, Fig. S7 *A*, *C*, and *D*). However, from a mechanistic point of view, this value of f_-^0/f_+^0 implied that interaction of microtubules with the cortex resulted in net pushing forces (*SI Appendix*, Fig. S7*B*), in contrast to the situation examined previously in which only pulling forces

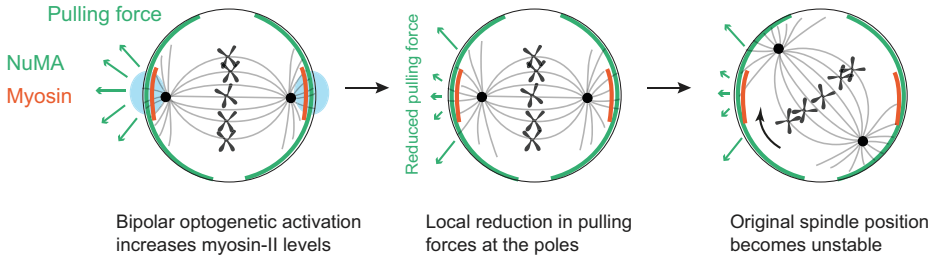

Fig. 6. Schematic model depicting the biophysical mechanism of spindle rotation observed after bipolar activation of Arhgef1-DH-PH in metaphase. *Left*, The spindle is initially in a stable position controlled by pulling forces (green) exerted on astral microtubules. Optogenetic activation at the poles (blue) results in local enrichment of myosin (red) at these regions. *Middle*, Increased cortical tension at the poles generated by myosin enrichment leads to a local reduction in the pulling force exerted on astral microtubules. *Right*, This change in force balance causes the original spindle position to become unstable. As the distribution of NuMA at the poles is broader than the activated region and not perturbed after activation, pulling forces powered by dynein/NuMA will exert a torque on the spindle, causing spindle rotation. The spindle rotates toward its new stable position where the cell undergoes anaphase and divides.

acted on the spindle (*SI Appendix*, Fig. S6*I*). Given that we did not observe inward movement of the centrosomes in response to optogenetic activation in the presence of MLN-8237 (Fig. 4 *C* and *E*) and that spindle rotation was abolished following treatment with Ciliobrevin D (Fig. 3*B*), such pushing forces would have to be dependent on the activity of NuMA and dynein, a mechanism not supported by current knowledge of spindle positioning.

The model allowed us to predict not only the average position of the spindle, but also the probability density function $p(t,\phi))$ of the spindle orientation at time t. To test how this probability changed with a given perturbation, we plotted the probability density function from the model for our three conditions at different times (Fig. 5*E*) and compared these with the experimentally observed probability distributions (Fig. 5 *F*–*H*). We found that under control conditions the distribution of spindle orientations remained steady over time and was peaked around 0° (Fig. 5*E*, control). Over 12 min, $p(t,\phi))$ split into two symmetric peaks in response to bipolar activation, whereas $p(t,\phi))$ retained a single peak that broadened slightly in response to global activation (Fig. 5*E*, bipolar, global). These model predictions were in good qualitative agreement with our experimental probability distributions, computed preactivation, 14 min postactivation, and at anaphase onset for all three conditions (Fig. 5 *F*–*H*). However, the distribution of spindle orientations in response to global activation displayed more extensive broadening under our experimental conditions than in the simulations.

Overall, our model predicted that a reduction of pulling force in myosin-enriched regions can cause the spindle to become unstable, rotating away from its initial stable position. Taken together, our model and experiments argue that spindle orientation can be understood from the interplay between cortical mechanics and the spindle positioning machinery.

Discussion

In this study, we have shown that mitotic spindles can change their orientation in response to inhomogeneities in myosin abundance and cortical tension, thereby affecting the axis of cell division. In our experiments, we increased cortical tension by activating RhoA via the optogenetic relocalization of GEF DH-PH. Recruitment of the GEF specifically to polar cortical regions in metaphase led to myosin enrichment in these regions, a local increase in cortical tension, and subsequent rotation of the spindle away from the cell poles. Whereas pulling forces mediated by cortical NuMA/dynein are essential to power rotation, their enrichment at the poles does not change upon GEF recruitment. Instead, our data suggest that a local reduction in the pulling force exerted on astral microtubules in tensed, myosin-rich regions destabilizes the spindle from its original position. The larger pulling force exerted by NuMA/dynein outside the region of activation generates a torque on the spindle leading to its rotation. A mathematical model incorporating this change in the force balance can qualitatively predict the spindle orientation distributions and rotation dynamics observed in experiments. Taken together, our data suggest that spindle reorientation in response to localized mechanical changes in the cortex is an emergent property of the interaction between the cortex and the spindle positioning machinery (Fig. 6).

Spindle Reorientation is an Emergent Property of the Interplay between Cortical Mechanics and the Spindle Positioning Machinery. Our model and experiments suggest that spindle rotation in response to a change in RhoA activity and cortical tension represents an emergent property of the interaction between the spindle positioning machinery and the cortex, rather than resulting from mechanotransductory signaling pathways. Indeed, our optogenetic activation experiments along with our laser ablation data indicate that a localized increase in cortical tension caused by myosin recruitment at the poles decreases pulling forces on the centrosomes. Our theoretical model can predict spindle rotation away from its initial stable position, simply by assuming that the experimentally measured myosin activation profile results in a reduction of cortical pulling forces. Although our current model is in qualitative agreement with our experiments, the magnitude of the rotation it predicts was smaller than our observations and the time scale necessary for rotation was shorter than in experiments. One potential reason for the shorter duration of rotation is that our model assumes that the distribution of pulling forces is immediately changed by optogenetic activation, whereas in our experiments signaling downstream of RhoA likely introduced a time lag. A potential source for the discrepancy in the magnitude of rotation is that although our experiments suggest a reduction of pulling forces in myosin-rich tensed regions, we currently lack a detailed characterization of how myosin contractility and tension impinge on the profile of pulling forces generated by dynein. In addition, forces generated by hydrodynamic interactions of moving dynein motors with the viscous cytoplasm may also contribute to spindle positioning, as in sea urchin embryos (56, 57). Moreover, we do not know whether and how increased cortical tension affects the number, density, or dynamics of astral microtubules, which will impact cortical pushing forces and forces generated by dynein movement along microtubules, both of which may participate in spindle rotation. In line with our experiments, our simulations only incorporated net reduction in pulling forces; however, if net pushing forces were present, then our model indicated that spindles would rotate to a new stable position of 90° rather than ~20° (*SI Appendix*, *Supplementary Theory* and Fig. S7*A*). Interestingly, the torque and velocity of rotation depended on the relative magnitude of pushing forces compared with pulling forces. When pushing forces were comparable or larger than pulling forces, the

time necessary to reach steady-state orientation became several times larger than the median time until anaphase onset, potentially limiting how far spindles can rotate away from their initial orientation (*SI Appendix*, *Supplementary Theory* and Fig. S7 *B–E*). It will be interesting to investigate the applicability of our model to organisms in which microtubule pushing has been evidenced, such as *Caenorhabditis elegans* (45). Within the framework of our model, spindles could, in principle, also reorient out of plane. However, we never observed out-of-plane reorientations in our experiments, and it will be interesting to determine why spindle rotation is constrained to the horizontal plane.

How tensed, myosin-enriched cortical regions generate less pulling force on astral microtubules is not understood. In addition, it is unclear whether myosin enrichment or increased tension causes reorientation. Although blebbistatin treatment prevents myosin force generation, it does not prevent myosin binding strongly to F-actin (58, 59). As blebbistatin abolished spindle rotation, this suggests that spindles do not respond to myosin enrichment alone but likely to a change induced by myosin force generation and increased cortical tension. An increase in myosin contractility and cortical tension may lead to a more tensed or rigid cortex, causing a reduced efficiency of force generation by dynein and/or a decrease in the lifetime of dynein–astral microtubule interaction, thereby reducing the average pulling force per astral microtubule. Alternatively, myosin contractility and increased cortical tension at the poles may change cortical thickness or cortex architecture by, e.g., reducing the average size of gaps within the cortical F-actin mesh. Such a reduction in mesh size may prevent astral microtubules from reaching the plasma membrane where the Gαi-LGN-NuMA-dynein complex is located, again leading to a reduction in the average pulling force per astral microtubule. Future experiments will be necessary to determine the biophysical mechanism through which cortical tension and/or myosin enrichment reduce pulling forces and/or affect pushing forces.

Inhomogeneities in Cortical Tension Control Spindle Orientation. Previous work has revealed that spindle orientation is sensitive to dynamic changes in the stress applied to dividing cells (14, 17, 20). However, little is known about the subcellular mechanical changes that cause reorientation. In our experiments, spindle reorientation was induced by a localized increase in RhoA activity at the poles, which led to a localized change in myosin contractility and a localized increase in cortical tension. A polar increase in myosin contractility leads to a localized increase in cortical tension, giving rise to a change in the cellular shape, a cue known to influence the orientation of cell division (31). However, bipolar activation led to only a small change in shape, a ∼3% decrease in the P/E ratio (*SI Appendix*, Fig. S1*E*). Since previous experimental and computational work showed that spindle orientation is strongly influenced by shape cues (31–33), we focused on quasi-spherical mitotic cells (P/E ratio, 0.85 to 1.25) to examine the impact of inhomogeneous cortical tension on spindle orientation with minimum contribution from shape cues. Under our experimental conditions, we did not find any correlation between the final spindle rotation angle and cell shape or changes in cell shape following optogenetic activation (*SI Appendix*, Fig. S1 *F* and *G*). Therefore, we suggest that spindles likely sense inhomogeneities in cortical tension possibly directly because of differences in myosin activity, and they rotate away from regions of high tension. However, we cannot completely rule out a potential influence of cell shape in our experiments. In the future, it will be interesting to carefully dissect the competition between shape cues, controlled with micropatterning, and inhomogeneous cortical tension, induced by optogenetics, in governing spindle orientation. Because it was tuned to our experimental conditions, our model only considered circular cells. However, in the future, it will be informative to implement arbitrary cell shapes since noncircular shapes will influence the torque distribution on the spindle, leading to a complex interplay between shape cues and cortical tension profiles (31, 33).

In living tissues, tension can arise from either active or passive processes. Active stress originates from the action of myosin motors on the cytoskeleton, whereas passive stress arises from the deformation of cytoskeletal networks in response to external forces. While in our experiments cortical tension inhomogeneities were generated through differences in active stress due to myosin enrichment, spindles have also been shown to reorient in response to passive stress arising from the application of a uniaxial stretch to isolated cells and tissues (14, 17). Isolated metaphase cells seeded on elliptical micropatterns have been stretched along their short axis, rendering the cells spherical. Spindles that were initially oriented along the long axis of the cell reoriented with an angle of ∼40° in ∼15 to 20 min before entering anaphase, similar to our experiments (17). Similarly, in the zebrafish enveloping layer, the application of an ectopic tissue stress perpendicular to the long axis of a dividing cell resulted in spindle reorientation with an angle of ∼30° within 6 to 7 min (14). In both studies, the likely result of mechanical manipulations was to increase cortical tension at the poles of the mitotic cell. Interestingly, the dynamics and magnitude of spindle reorientation in these studies are comparable to our data, suggesting that reorientation may be independent of the exact process through which cortical tension inhomogeneity is generated.

Physiological Consequence of Spindle Rorientation. Reorientation of mitotic spindles in response to a sudden application of stress may help optimize cell packing in tissues subjected to deformations as part of their physiological function (60) or in organ development where mechanical stresses play an integral part in guiding further morphogenesis (61–63). While previous studies have examined the orientation of cell divisions in response to a constant stretch lasting several hours (6, 14, 23), many epithelial tissues such as the skin, bladder, or intestine are subjected to transient deformations, which generate transient inhomogeneous stress fields. Our study indicates that despite their transient nature, these stresses may be sufficient to reorient the axis of division of metaphase cells. Such a phenomenon may allow the tissue to optimize its organization to reduce stress in the direction of extension.

Materials and Methods

Generation of Optogenetic Cell Lines. All stable cell lines expressing the optogenetic constructs and the reporter constructs were made either by retroviral or lentiviral transductions, or by electroporation into MDCKII cells.

Sample Preparation and Optogenetic Activation. For all optogenetic experiments, ∼50,000 cells were plated on 35 mm glass-bottom dishes ∼36 h prior to imaging. Activation experiments were carried out on an Olympus FV-1200 confocal microscope, using the 473 nm light set at 2% laser power. Defined regions of interest were illuminated for 350 ms every 2 min until the end of cell division. Images were acquired in the medial focal plane of the dividing cell with a 30 s time interval taken from metaphase until the end of cell division. A full description of materials and methods can be found in *SI Appendix*.

Data Availability. Data, analysis files, and simulation codes have been deposited in the University College London data repository and can be accessed at https://rdr.ucl.ac.uk/ (DOI: 10.5522/04/16871626) (64).

ACKNOWLEDGMENTS. We thank Susana Godinho (Queen Mary University of London, United Kingdom) for gateway cloning plasmids; Mathieu Coppey (Institut Curie, Paris, France) for advice on optogenetics and sharing reagents; Ayad

Eddaoudi (University College London, Institute for Child Health) for flow cytometry analysis; Jonathan Fouchard, Julia Duque, Kazunori Yamamoto, and Diana Khoromskaia for comments and discussions; and members of the G.C. and B.B. laboratories for discussions. M.K. was supported by a Swiss National Science Foundation early postdoctoral fellowship (P2LAP3_164919) and by a European Research Council consolidator grant (CoG-647186) to G.C. P.B. was supported by a Cancer Research UK multidisciplinary award (C55977/A23342) to G.C. and G.S. M.B.S. and G.S. were supported by the Francis Crick Institute, which receives its core funding from Cancer Research UK (FC001317), the UK Medical Research Council (FC001317), and the Wellcome Trust (FC001317).

Author affiliations: [a]London Centre for Nanotechnology, University College London, London WC1H 0AH, United Kingdom; [b]The Francis Crick Institute, London NW1 1AT, United Kingdom; [c]Centre for Developmental Neurobiology, Institute of Psychiatry, Psychology and Neuroscience, King's College London, London SE1 1UL, United Kingdom; [d]Medical Research Council Centre for Neurodevelopmental Disorders, King's College London, London SE1 1UL, United Kingdom; [e]Department of Developmental and Stem Cell Biology, Institut Pasteur, CNRS UMR 3738, 75015 Paris , France; [f]Medical Research Council Laboratory for Molecular Cell Biology, University College London, London WC1E 6BT, United Kingdom; [g]Division of Cell Biology, Medical Research Council Laboratory of Molecular Biology, Cambridge CB2 0QH, United Kingdom; [h]Institute for the Physics of Living Systems, University College London, London WC1E 6BT, United Kingdom; [i]Department of Genetics and Evolution, Quai Ernest-Ansermet 30, 1205 Geneva, Switzerland; and [j]Department of Cell and Developmental Biology, University College London, London WC1E 6BT, United Kingdom

1. E. G. Conklin, Effects of centrifugal force on the polarity of the eggs of Crepidula. *Proc. Natl. Acad. Sci. U.S.A.* **2**, 87–90 (1916).
2. R. Rappaport, Experiments concerning the cleavage stimulus in sand dollar eggs. *J. Exp. Zool.* **148**, 81–89 (1961).
3. P. Gönczy, Mechanisms of asymmetric cell division: Flies and worms pave the way. *Nat. Rev. Mol. Cell Biol.* **9**, 355–366 (2008).
4. S. E. Williams, E. Fuchs, Oriented divisions, fate decisions. *Curr. Opin. Cell Biol.* **25**, 749–758 (2013).
5. X. Morin, Y. Bellaïche, Mitotic spindle orientation in asymmetric and symmetric cell divisions during animal development. *Dev. Cell* **21**, 102–119 (2011).
6. T. P. Wyatt *et al.*, Emergence of homeostatic epithelial packing and stress dissipation through divisions oriented along the long cell axis. *Proc. Natl. Acad. Sci. U.S.A.* **112**, 5726–5731 (2015).
7. W. T. Gibson *et al.*, Control of the mitotic cleavage plane by local epithelial topology. *Cell* **144**, 427–438 (2011).
8. Z. Zheng *et al.*, LGN regulates mitotic spindle orientation during epithelial morphogenesis. *J. Cell Biol.* **189**, 275–288 (2010).
9. E. Peyre *et al.*, A lateral belt of cortical LGN and NuMA guides mitotic spindle movements and planar division in neuroepithelial cells. *J. Cell Biol.* **193**, 141–154 (2011).
10. L. A. Baena-López, A. Baonza, A. García-Bellido, The orientation of cell divisions determines the shape of Drosophila organs. *Curr. Biol.* **15**, 1640–1644 (2005).
11. B. Aigouy *et al.*, Cell flow reorients the axis of planar polarity in the wing epithelium of Drosophila. *Cell* **142**, 773–786 (2010).
12. F. Lázaro-Diéguez, I. Ispolatov, A. Müsch, Cell shape impacts on the positioning of the mitotic spindle with respect to the substratum. *Mol. Biol. Cell* **26**, 1286–1295 (2015).
13. F. Bosveld *et al.*, Epithelial tricellular junctions act as interphase cell shape sensors to orient mitosis. *Nature* **530**, 495–498 (2016).
14. P. Campinho *et al.*, Tension-oriented cell divisions limit anisotropic tissue tension in epithelial spreading during zebrafish epiboly. *Nat. Cell Biol.* **15**, 1405–1414 (2013).
15. M. Gloerich, J. M. Bianchini, K. A. Siemers, D. J. Cohen, W. J. Nelson, Cell division orientation is coupled to cell-cell adhesion by the E-cadherin/LGN complex. *Nat. Commun.* **8**, 13996 (2017).
16. E. Scarpa, C. Finet, G. B. Blanchard, B. Sanson, Actomyosin-driven tension at compartmental boundaries orients cell division independently of cell geometry in vivo. *Dev. Cell* **47**, 727–740.e6 (2018).
17. J. Fink *et al.*, External forces control mitotic spindle positioning. *Nat. Cell Biol.* **13**, 771–778 (2011).
18. M. Théry *et al.*, The extracellular matrix guides the orientation of the cell division axis. *Nat. Cell Biol.* **7**, 947–953 (2005).
19. A. Dimitracopoulos *et al.*, Mechanochemical crosstalk produces cell-intrinsic patterning of the cortex to orient the mitotic spindle. *Curr. Biol.* **30**, 3687–3696.e4 (2020).
20. M. S. Y. Lam *et al.*, Isotropic myosin-generated tissue tension is required for the dynamic orientation of the mitotic spindle. *Mol. Biol. Cell* **31**, 1370–1379 (2020).
21. E. V. van Leen, F. di Pietro, Y. Bellaïche, Oriented cell divisions in epithelia: From force generation to force anisotropy by tension, shape and vertices. *Curr. Opin. Cell Biol.* **62**, 9–16 (2020).
22. K. C. Hart *et al.*, E-cadherin and LGN align epithelial cell divisions with tissue tension independently of cell shape. *Proc. Natl. Acad. Sci. U.S.A.* **114**, E5845–E5853 (2017).
23. A. Nestor-Bergmann *et al.*, Decoupling the roles of cell shape and mechanical stress in orienting and cueing epithelial mitosis. *Cell Rep.* **26**, 2088–2100.e4 (2019).
24. M. J. Kennedy *et al.*, Rapid blue-light-mediated induction of protein interactions in living cells. *Nat. Methods* **7**, 973–975 (2010).
25. L. Valon, A. Marín-Llaudaó, T. Wyatt, G. Charras, X. Trepat, Optogenetic control of cellular forces and mechanotransduction. *Nat. Commun.* **8**, 14396 (2017).
26. M. J. Hart *et al.*, Identification of a novel guanine nucleotide exchange factor for the Rho GTPase. *J. Biol. Chem.* **271**, 25452–25458 (1996).
27. L. Valon *et al.*, Predictive spatiotemporal manipulation of signaling perturbations using optogenetics. *Biophys. J.* **109**, 1785–1797 (2015).
28. S. P. Ramanathan *et al.*, Cdk1-dependent mitotic enrichment of cortical myosin II promotes cell rounding against confinement. *Nat. Cell Biol.* **17**, 148–159 (2015).
29. P. Chugh *et al.*, Actin cortex architecture regulates cell surface tension. *Nat. Cell Biol.* **19**, 689–697 (2017).
30. M. Kelkar, P. Bohec, G. Charras, Mechanics of the cellular actin cortex: From signalling to shape change. *Curr. Opin. Cell Biol.* **66**, 69–78 (2020).
31. J. Li, L. Cheng, H. Jiang, Cell shape and intercellular adhesion regulate mitotic spindle orientation. *Mol. Biol. Cell* **30**, 2458–2468 (2019).
32. S. Chanet, R. Sharan, Z. Khan, A. C. Martin, Myosin 2-induced mitotic rounding enables columnar epithelial cells to interpret cortical spindle positioning cues. *Curr. Biol.* **27**, 3350–3358.e3 (2017).
33. N. Minc, D. Burgess, F. Chang, Influence of cell geometry on division-plane positioning. *Cell* **144**, 414–426 (2011).
34. A. J. Piekny, M. Glotzer, Anillin is a scaffold protein that links RhoA, actin, and myosin during cytokinesis. *Curr. Biol.* **18**, 30–36 (2008).
35. T. Matsui *et al.*, Rho-associated kinase, a novel serine/threonine kinase, as a putative target for small GTP binding protein Rho. *EMBO J.* **15**, 2208–2216 (1996).
36. M. Amano *et al.*, Phosphorylation and activation of myosin by Rho-associated kinase (Rho-kinase). *J. Biol. Chem.* **271**, 20246–20249 (1996).
37. K. Kimura *et al.*, Regulation of myosin phosphatase by Rho and Rho-associated kinase (Rho-kinase). *Science* **273**, 245–248 (1996).
38. S. Narumiya, T. Ishizaki, N. Watanabe, Rho effectors and reorganization of actin cytoskeleton. *FEBS Lett.* **410**, 68–72 (1997).
39. M. Bovellan *et al.*, Cellular control of cortical actin nucleation. *Curr. Biol.* **24**, 1628–1635 (2014).
40. M. Maekawa *et al.*, Signaling from Rho to the actin cytoskeleton through protein kinases ROCK and LIM-kinase. *Science* **285**, 895–898 (1999).
41. C. Lucas-Lopez *et al.*, The small molecule tool (S)-(-)-blebbistatin: Novel insights of relevance to myosin inhibitor design. *Org. Biomol. Chem.* **6**, 2076–2084 (2008).
42. E. Fischer-Friedrich *et al.*, Rheology of the active cell cortex in mitosis. *Biophys. J.* **111**, 589–600 (2016).
43. S. Kotak, C. Busso, P. Gönczy, Cortical dynein is critical for proper spindle positioning in human cells. *J. Cell Biol.* **199**, 97–110 (2012).
44. Q. Du, I. G. Macara, Mammalian Pins is a conformational switch that links NuMA to heterotrimeric G proteins. *Cell* **119**, 503–516 (2004).
45. C. Garzon-Coral, H. A. Fantana, J. Howard, A force-generating machinery maintains the spindle at the cell center during mitosis. *Science* **352**, 1124–1127 (2016).
46. I. M. Tolić-Nørrelykke, Push-me-pull-you: How microtubules organize the cell interior. *Eur. Biophys. J.* **37**, 1271–1278 (2008).
47. S. W. Grill, A. A. Hyman, Spindle positioning by cortical pulling forces. *Dev. Cell* **8**, 461–465 (2005).
48. M. Dogterom, J. W. Kerssemakers, G. Romet-Lemonne, M. E. Janson, Force generation by dynamic microtubules. *Curr. Opin. Cell Biol.* **17**, 67–74 (2005).
49. A. J. Firestone *et al.*, Small-molecule inhibitors of the AAA+ ATPase motor cytoplasmic dynein. *Nature* **484**, 125–129 (2012).
50. S. Gallini *et al.*, NuMA phosphorylation by aurora-A orchestrates spindle orientation. *Curr. Biol.* **26**, 458–469 (2016).
51. M. Okumura, T. Natsume, M. T. Kanemaki, T. Kiyomitsu, Dynein-dynactin-NuMA clusters generate cortical spindle-pulling forces as a multi-arm ensemble. *eLife* **7**, e36559 (2018).
52. S. W. Grill, P. Gönczy, E. H. Stelzer, A. A. Hyman, Polarity controls forces governing asymmetric spindle positioning in the Caenorhabditis elegans embryo. *Nature* **409**, 630–633 (2001).
53. A. M. Corrigan, R. Shrestha, V. M. Draviam, A. M. Donald, Modeling of noisy spindle dynamics reveals separable contributions to achieving correct orientation. *Biophys. J.* **109**, 1398–1409 (2015).
54. M. Théry, A. Jiménez-Dalmaroni, V. Racine, M. Bornens, F. Jülicher, Experimental and theoretical study of mitotic spindle orientation. *Nature* **447**, 493–496 (2007).
55. M. Bjerknes, Physical theory of the orientation of astral mitotic spindles. *Science* **234**, 1413–1416 (1986).
56. J. Xie *et al.*, Contribution of cytoplasm viscoelastic properties to mitotic spindle positioning. *Proc. Natl. Acad. Sci. U.S.A.* **119**, e2115593119 (2022).
57. H. Palenzuela *et al.*, In vitro reconstitution of dynein force exertion in a bulk viscous medium. *Curr. Biol.* **30**, 4534–4540.e7 (2020).
58. G. T. Charras, C. K. Hu, M. Coughlin, T. J. Mitchison, Reassembly of contractile actin cortex in cell blebs. *J. Cell Biol.* **175**, 477–490 (2006).
59. B. Takács *et al.*, Myosin complexed with ADP and blebbistatin reversibly adopts a conformation resembling the start point of the working stroke. *Proc. Natl. Acad. Sci. U.S.A.* **107**, 6799–6804 (2010).
60. J. Liang, S. Balachandra, S. Ngo, L. E. O'Brien, Feedback regulation of steady-state epithelial turnover and organ size. *Nature* **548**, 588–591 (2017).
61. E. Steed, F. Boselli, J. Vermot, Hemodynamics driven cardiac valve morphogenesis. *Biochim. Biophys. Acta* **1863** (7 Pt B), 1760–1766 (2016).
62. R. T. Martin, T. Bartman, Analysis of heart valve development in larval zebrafish. *Dev. Dyn.* **238**, 1796–1802 (2009).
63. L. Andrés-Delgado, N. Mercader, Interplay between cardiac function and heart development. *Biochim. Biophys. Acta* **1863** (7 Pt B), 1707–1716 (2016).
64. M. Kelkar et al., Spindle reorientation in response to mechanical stress is an emergent property of the spindle positioning mechanisms. University College London. Dataset. https://doi.org/10.5522/04/16871626. Deposited 15 June 2022.